Band structure and thermoelectric properties of half-Heusler semiconductors from many-body perturbation theory

Maedeh Zahedifar and Peter Kratzer
Fakultät für Physik, Universität Duisburg-Essen, Campus Duisburg, Lotharstr. 1, 47057 Duisburg, Germany

(Received 15 December 2017; published 24 January 2018)

Various *ab initio* approaches to the band structure of ANiSn and ACoSb half-Heusler compounds (A = Ti, Zr, Hf) are compared and their consequences for the prediction of thermoelectric properties are explored. Density functional theory with the generalized-gradient approximation (GGA), as well as the hybrid density functional HSE06 and *ab initio* many-body perturbation theory in the form of the GW_0 approach, are employed. The GW_0 calculations confirm the trend of a smaller band gap (0.75 to 1.05 eV) in ANiSn compared to the ACoSb compounds (1.13 to 1.44 eV) already expected from the GGA calculations. While in ANiSn materials the GW_0 band gap is 20% to 50% larger than in HSE06, the fundamental gap of ACoSb materials is smaller in GW_0 compared to HSE06. This is because GW_0, similar to PBE, locates the valence band maximum at the L point of the Brillouin zone, whereas it is at the Γ point in the HSE06 calculations. The differences are attributed to the observation that the relative positions of the d levels of the transition metal atoms vary among the different methods. Using the calculated band structures and scattering rates taking into account the band effective masses at the extrema, the Seebeck coefficients, thermoelectric power factors, and figures of merit ZT are predicted for all six half-Heusler compounds. Comparable performance is predicted for the n-type ANiSn materials, whereas clear differences are found for the p-type ACoSb materials. Using the most reliable GW_0 electronic structure, ZrCoSb is predicted to be the most efficient material with a power factor of up to 0.07 $\mathrm{W/(K^2\,m)}$ at a temperature of 600 K. We find strong variations among the different *ab initio* methods not only in the prediction of the maximum power factor and ZT value of a given material, but also in comparing different materials to each other, in particular in the p-type thermoelectric materials. Thus we conclude that the most elaborate, but also most costly GW_0 method is required to perform a reliable computational search for the optimum material.

DOI: 10.1103/PhysRevB.97.035204

I. INTRODUCTION

First-principles computational methods have developed into standard tools in materials science in recent years. Most of the work is carried out using density functional theory in its local or semilocal form, while the computationally demanding methods of many-body perturbation theory (MBPT), the GW approximation and the Bethe-Salpeter equation, are employed only when the optical properties of a material are in the focus of interest. In this paper, we critically discuss the validity of first-principles methods, including hybrid functionals and MBPT, for thermoelectric materials, and show that the conclusions drawn from GW_0 calculations are substantially different from those based on less computationally expensive approaches.

For predicting the thermoelectric properties of a material, knowledge of its electronic properties is of utmost importance. Not only the band gap, but also the structure of the valence band maxima (VBM) and conduction band minima (CBM), i.e., the multiplicity of VBM and CBM, the degeneracy of bands and band dispersion, enter into the numerical expression for the thermoelectric power factor. For wide-gap materials that are used as strongly doped electrodes in unipolar devices, the curvature of the bands in a region of about $5k_BT$ above the CBM (below VBM) determines the thermoelectric transport properties of the n-type (p-type) material. It is known from conventional semiconductors that the effective mass tensor, given by the inverse of the band curvature, is often not correctly reproduced (compared to experimental values) in DFT calculations, whereas many-particle calculations within the GW approach are found to give excellent agreement with experimentally derived band parameters, e.g., for silicon [1,2] and group-III nitride semiconductors [3]. In contrast to these elemental and binary semiconductors, in the ternary semiconductors of interest for thermoelectrics, experimental data on the effective masses of the carriers are hardly available. Therefore reliable theoretical studies of their electronic structure using many-particle techniques are of timely interest.

For harvesting waste heat at elevated temperatures ($T >$ 400 K), ternary materials with crystal structure $C1_b$, so-called half-Heusler alloys [4], have attracted much attention due their high thermal stability and their environmental friendliness. In recent years, numerous papers have been published that attempt to identify materials with optimized electronic structure for highest thermoelectric performance. For instance, numerous half-Heusler compounds [5] have been screened computationally. In the quest for materials with a high thermoelectric power factor, descriptors frequently discussed in the literature [6,7] are the multiplicity of degenerate band extrema contributing to the transport (with large multiplicity implying high thermopower) and the band curvature (flat versus highly dispersive bands) closely related to the effective masses. From a fundamental perspective, a narrow, flat conductive band should yield optimum thermoelectric performance since the entropy transported per charge carrier is minimal [8]. However,

 ©2018 American Physical Society

for a material to be used technologically, in addition to a large thermopower, also a high electrical conductivity is required. In addition to the concentration of carriers, which must be tuned via suitable doping, a high mobility, and thus a low effective mass in transport direction, is a prerequisite. While these two points of view pose contradictory demands on a thermoelectric material, the often decisive factor in practice is the thermal conductivity, a quantity that is dominated by the lattice contribution in most semiconducting materials. In materials with small lattice (and total) thermal conductivity, the aspect of minimum entropy per carrier will prevail and dominate the overall performance, whereas in materials with a considerable thermal conductivity, a good electrical conductivity is required as well in order to ensure a good thermoelectric performance. In the $C1_b$ semiconductors of interest to us, at least in samples with high crystalline quality, the lattice thermal conductivity is considerable, typically in the range of 15–25 W/Km at room temperature in pure samples [9–12]. In technically used samples, however, the thermal conductivity is often reduced by almost one order of magnitude due to doping or alloying. Even so, achieving a high electrical conductivity and high power factor is mandatory for the use of these materials in thermoelectrics, as will be shown below. Recently, a computational search for p-type half-Heusler alloys with low effective mass has been performed on the DFT level of theory [13].

In this paper, we study six half-Heusler materials with chemical formula ANiSn or ACoSb, where A is an element of group IVb (Ti, Zr or Hf). In all six materials, the overall valence electron count is 18, and consequently all materials are semiconductors. In chemical language, the group IVb element A is characterized by high-lying atomic orbitals ($3d$, $4d$, or $5d$ orbitals) and hence has the ability to transfer charge to the main group element (Sn or Sb). From the perspective of thermoelectrics, the ANiSn compounds possess conduction band minima at the X point and are used in n-doped form. The ACoSb compounds are used in p-doped form; the location of their hole carriers pockets in the Brillouin zone is still up to debate, see the discussion below. In order to achieve high electrical conductivity, an efficient doping strategy must be at hand. Here, it needs to be noted that many ternary compounds display natural off-stoichiometry [14] and, thus, are intrinsically doped. For example, Ni interstitials may be formed under a surplus of Ni in the ANiSn compounds [15,16], and these induce an impurity band in vicinity to the conduction-band edge. Extrinsic n-type doping may be realized by substituting the nonmetal position of the lattice, i.e., by substituting Sn by Sb [17]. In a similar manner, p-type doping in ACoSb compounds can be realized by substituting Sb by Sn [18,19]. Other possibilities of doping involve the substitution of the group-IVb lattice site by either a group-IIIb atom, e.g., Sc [20] or a group-Vb atom, e.g., Ta [21], V, or Nb [22].

In this work, we carry out computational investigations of the band structure of the six above-mentioned half-Heusler materials assuming pure, perfect crystals. The structure of the paper is as follows: first, we calculate the band structure of the materials using three different methods of increasing quality, but also increasing computational cost. We present Kohn-Sham band gaps obtained with (i) the GGA-PBE density functional, (ii) a generalized Kohn-Sham scheme (the HSE06 hybrid functional), and (iii) quasiparticle band gaps from many-body perturbation theory (GW_0). The position of band extrema and their associated effective-mass tensors are evaluated. In a second step, we calculate the thermoelectric properties from the band structure data using Boltzmann transport theory. The electronic relaxation time τ is described by an energy-dependent scattering rate that includes the effective masses. Finally, the power factor σS^2 and, assuming constant lattice thermal conductivity κ_{lat}, the figure of merit $ZT = \sigma S^2/(\kappa_{\text{el}} + \kappa_{\text{lat}})$ are calculated as a function of the carrier concentration. We conclude by pointing out the consequences of our work for real materials.

II. COMPUTATIONAL METHODOLOGY AND BASIC MATERIALS PROPERTIES

In this work, the GW_0, HSE06, and PBE-GGA calculations are carried out with the projector augmented-wave method and the software package VASP [23,24]. For the DFT part we use both the Perdew-Burke-Ernzerhof (PBE [25]) formulation of the generalized gradient (GGA) and the HSE06 [26,27] functionals for calculating the exchange-correlation potential. The DFT calculations are performed on a $16 \times 16 \times 16$ Monkhorst-Pack **k**-point grid with 145 **k** points in the irreducible wedge to obtain a reliable starting point. The GW_0 and HSE06 calculations are performed with a $7 \times 7 \times 7$ **k**-point mesh with a cut-off energy of 400 eV for the wave functions. For all group-IVb elements, the electrons in the highest occupied p shell were treated as valence electrons, e.g., for Hf the pseudopotential included the $5p$, $6s$, and $5d$ electrons as valence states. For Ti and Zr, the $3s$ and $4s$ electrons, respectively, were added to the valence in order to describe the polarizability of these semicore states. For Co and Ni, the $3d$ and $4s$ electrons were treated as valence electrons, while for Sn and Sb, the valence configuration is $5s^25p^2$ and $5s^25p^3$, respectively. For getting band structures, the WANNIER90 code [28] was used to interpolate between **k** points using maximally localized Wannier functions.

For calculating the thermoelectric properties, the BOLTZTRAP code [29] was employed. Doping is treated within the rigid band approximation [30]. For the electronic transport relaxation time τ, the following model [31] is used:

$$\tau(E,T) = \tau_0 \times \left(\frac{|E - E_{\text{VBM/CBM}}|}{k_B T}\right)^{-1/2} \left(\frac{T_0}{T}\right)^{-1/2}, \quad (1)$$

where E_{VBM} and E_{CBM} are the valence band maximum or conduction band minimum in case of p-type or n-type conduction, respectively, and $T_0 = 300$ K is the reference temperature for which τ_0 is specified.

First, we obtain optimized lattice constants for all six compounds, using the PBE or HSE06 functionals. The results are collected in Table I and compared to the experimental values. The PBE pseudopotential calculations overestimate the lattice constant by 1% (ZrNiSn), 2% (HfNiSn),4% (HfCoSb), 2% (TiNiSn), and 3% (TiCoSb), while the HSE06 calculations slightly underestimate the lattice constants. For ZrCoSb, both the PBE and HSE06 underestimate the lattice constant.

Electronic charge transfer and band formation in the semiconducting half-Heusler compounds have been discussed

TABLE I. Lattice constants in Å for ZrNiSn, ZrCoSb, HfNiSn, HfCoSb, TiNiSn, and TiCoSb using the PBE and the HSE06 functional, respectively. The experimental values are taken from Refs. [32,33].

	PBE	HSE06	experiment
ZrNiSn	6.15	6.12	6.11
ZrCoSb	6.06	6.04	6.07
HfNiSn	6.10	6.00	6.09
HfCoSb	6.07	6.02	6.04
TiNiSn	5.95	5.93	5.94
TiCoSb	5.90	5.86	5.88

on a qualitative level already in previous work (see, e.g., Refs. [16,34]). The nonmetal constituent (Sn or Sb) reaches closed-shell character by receiving four or three electrons, respectively, from the metal atoms. The band gap arises due to different hybridization between the d orbitals of the metallic constituents. Here, the group-IVb elements have the highest lying d orbitals. It is noteworthy that Ti is clearly distinct from Zr and Hf in this respect, since with the PBE functional the atomic $3d$ orbitals of a free Ti atom lie at -1.03 eV below the vacuum level, whereas the $4d$ and $5d$ electrons of Zr and Hf are more strongly bound (levels at -1.54 and -1.58 eV in Zr and Hf, respectively). For a comparison of the gross features of the electronic structure, the orbital projected density of states as obtained with the PBE functional for all six compounds is displayed in Fig. 1. In all materials, the states above and below the band gap have d-orbital character. In the group IVb element, the e_g states (e.g., the d_{z^2} state) are unoccupied, whereas the t_{2g} states hybridize with the states of the late transition metal (Co or Ni) and are partially occupied. Characteristic of the NiSn compounds are the relatively low-lying $3d$ states of Ni, located at -1.97 eV. These will later show up as an admixture to the dispersive branch of the conduction band reaching down from the Γ point to the X point. The conduction band minimum at X therefore contains about equal contributions from Ni $3d$ and group-IVb orbitals. The VBM in the NiSn compounds is almost exclusively of group-IVb character. This is in contrast to the CoSb-compounds, where in the valence bands the hybridization between Co orbitals (atomic level at -1.82 eV) and group-IVb orbitals is strong. In these materials, the Co orbital character is found to dominate at the CBM. Comparing the contributions of the different group-IVb atoms in ACoSb to the valence band, it is noteworthy that the degree of hybridization increases from Co–Ti (weak hybridization) over Co–Zr to Co–Hf (strong hybridization). This is related to the different energetic position and spatial extent of the $3d$, $4d$, and $5d$ orbitals. The Co $3d$ orbitals are energetically close to, and hence in resonance with, the Zr and Hf d orbitals. The consequence for the valence band structure will be discussed below.

A well-known problem of Kohn-Sham band structures obtained with (semi-)local DFT functionals is the too small fundamental band gap. By using modern hybrid DFT functionals, this shortcoming can be resolved for many elemental and binary semiconductors, while still reproducing good, or even improved, structural data. A frequently used hybrid functional is the Heyd-Scuseria-Ernzerhof (HSE06) functional [26,27] that mixes the DFT exchange potential with $\alpha = 25\%$ of screened exact exchange. In particular, in polar semiconductors with a charge-transfer gap, the mixing-in of exact exchange lowers the valence bands (having the orbital character of the anion) and lifts the conduction band states (having the orbital character of the cation), leading to larger band gaps [35] and thus to improved agreement with experiment. In the ternary semiconductors with $C1_b$ crystal structure studied in this paper, it is less obvious which method may be suitable to obtain an improved band gap: in these materials, the gap opens between two different linear combinations of d orbitals, i.e., it is a hybridization gap. While one would expect that a many-particle treatment of localized d states will lead to an energetic downshift of occupied states and an upshift of unoccupied states (on an absolute scale), it is unclear how these corrections would affect the band gap provided that *both* the CBM and the VBM have prevailing d-orbital character.

To clarify this point, a method independent of the mixing parameter α, such as the GW_0 approach, is desirable. For half-Heusler materials, we are only aware of one application of this method to TaCoSn [36], where a band gap of 1.3 eV was obtained, to be compared to the experimental onset of optical absorption at 1.6 eV. For related materials with hybridization gaps between d orbitals, e.g., the full-Heusler alloy of composition CoCrTiSb, a GW study [37] reported relatively small many-particle corrections to the band gap, presumably because concurrent shifts of both the VBM and CBM tend to cancel. We carried out GW_0 calculations based on the implementation of the frequency-dependent polarizability [38] in the VASP code. For the crystal structure, the experimental lattice constants have been used. The GW_0 calculation starts from the DFT (PBE) polarizability and calculates the screened interaction W_0, which in turn is used to determine the self-energy Σ with the Green function G_0 from DFT (PBE). Four iterations on the Green function were used to obtain converged results for the diagonal matrix elements of $\Sigma = iGW_0$. Such calculations are already pretty reliable for semiconductor band gaps, which are underestimated by the Kohn-Sham gaps of DFT calculations. Due to the energy (frequency) dependence of Σ, electron bands at different energies are under the influence of differently screened Coulomb interactions. Consequently, in most elemental or binary semiconductors, the conduction band is shifted upwards in an approximately rigid way. However, due to the wave-vector dependence of Σ, more profound changes of the band structure, e.g., such that the character of the band gap may change, are possible and indeed observed in the materials studied here.

III. RESULTS

A. Electronic structure

Band structures of all six compounds have been calculated in the scalar-relativistic approximation using the PBE, the HSE06 functional, and the GW_0 method. Since LDA or PBE band structures for these materials have been published previously, these are not shown, and we refer the reader to the literature (for ZrNiSn and ZrCoSb [20], for HfCoSb [39],

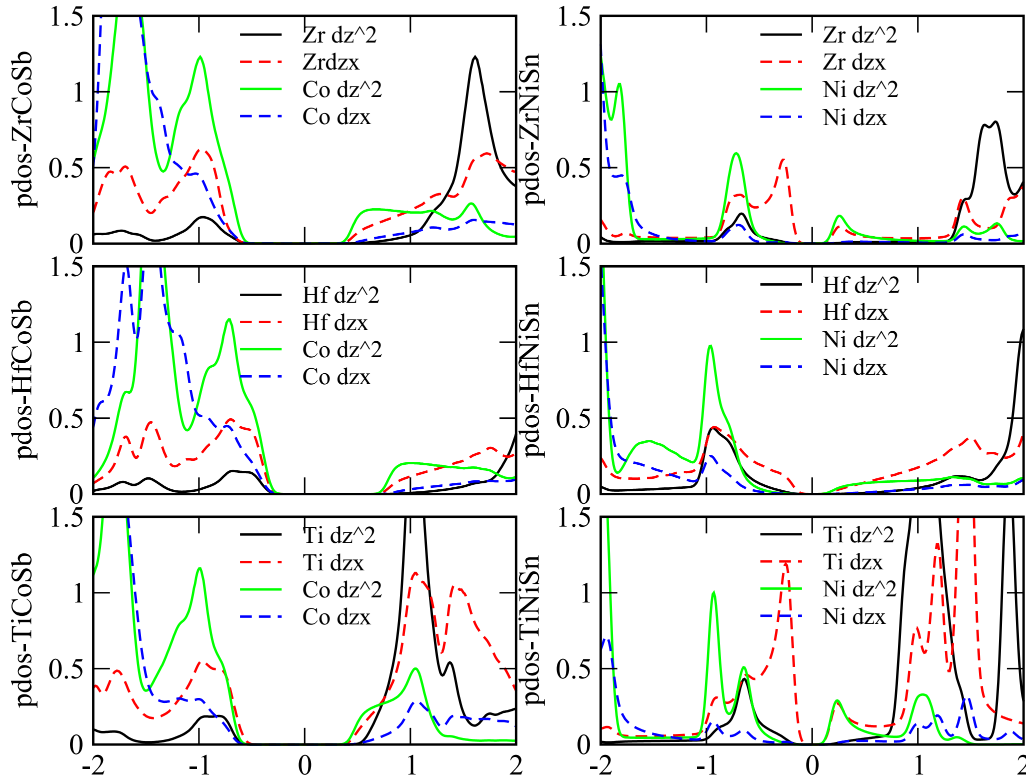

FIG. 1. Projected DOS from PBE-GGA calculations of the e_g and t_{2g} orbitals of the group-IVb metal and Co in ZrCoSb (upper panel left), the group-IVb metal and Ni in ZrNiSn (upper panel right), HfCoSb (middle panel left), HfNiSn (middle panel right), TiCoSb (lower panel left), and TiNiSn (lower panel right) around the band gap.

for TiNiSn [12,40,41], for HfNiSn [12,42], and for ZrNiSn [12,16,42]) for a comparison.

In addition, we carried out calculations within the VASP code including the spin-orbit coupling (SOC). While the qualitative features of band structures are the same with and without SOC, the effects of SOC become noticeable at high-symmetry points. The fivefold degenerate VBM at Γ gets split into a twofold and a threefold degenerate maximum. When moving away from the Γ point, these degeneracies are further lifted. The splitting at the Γ point amounts to 101 meV in HfNiSn and 69 meV in HfCoSb, and less than 1 meV in the other compounds. Thus the splitting is smaller than $k_B T$ for the light compounds containing Ti or Zr, while it becomes comparable to $k_B T$ for the compounds of the heavy element Hf. In the calculations of thermoelectric coefficients, an energy range of several $k_B T$ contributes. Therefore the thermoelectric quantities will be given by weighted averages over the split bands. We conclude that SOC in the compounds considered has only a minor effect on the thermoelectric properties. In the following, we continue to work in the scalar-relativistic approximation neglecting SOC. We note that the CBM at the X point remains degenerate even when SOC is included; thus the thermoelectric properties of n-type materials are unaffected by SOC.

The band structures obtained with the HSE06 functional are shown in Fig. 2. Band structures obtained with the HSE06 functional can also be found in Ref. [14]. The most important band structure data are summarized in Tables II–IV.

In the right column of Fig. 2, the band structures for the ANiSn materials are shown. These materials have an indirect band gap $\Gamma \rightarrow X$, which is qualitatively reproduced in all methods. Quantitatively, the band gap is only moderately increased in the HSE06 functional compared to the PBE functional, typically by 20% to 50%. Our results compare favorably with other HSE06 calculations in the literature for ZrNiSn [16,43] ($E_{\text{gap}} = 0.58$ and 0.60 eV, respectively) and for TiCoSb [44] ($E_{\text{gap}} = 1.45$eV). The band gap values quoted in

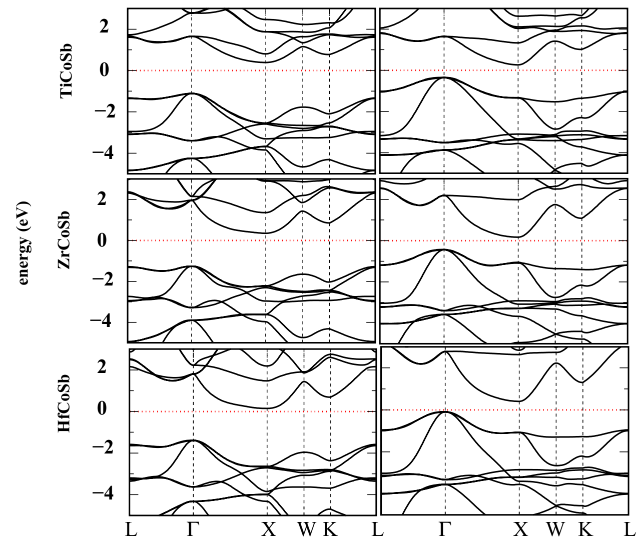

FIG. 2. HSE band structure.

TABLE II. Band gaps, conduction band effective masses $m_{X\to\Gamma}$ and $m_{X\to L}$, light and heavy hole masses m_{lh} and m_{hh} at Γ, and the hole masses at the L point for TiNiSn and TiCoSb, calculated with the PBE, HSE06 density functional, and the GW_0 method.

	TiNiSn			TiCoSb		
functional	PBE	HSE06	GW	PBE	HSE06	GW
$E_{\mathrm{gap}\Gamma-X}$	0.45	0.62	0.75	0.51	1.50	1.55
$E_{\mathrm{gap}L-X}$	0.88	1.29	1.12	0.92	1.72	1.32
$m_{X\to\Gamma}$	2.62	1.59	9.74	3.26	2.81	5.22
$m_{X\to W}$	0.53	0.35	1.06	1.77	1.01	2.18
$m_{lh,\Gamma\to L}$	0.22	0.40	0.30	0.31	0.27	0.55
$m_{lh,\Gamma\to X}$	0.39	0.72	0.55	0.50	0.53	0.78
$m_{h,L\to\Gamma}$	3.87	–	2.50	2.83	–	1.03
$m_{h,L\to K}$	0.55	–	1.16	0.45	–	0.81
$m_{hh,\Gamma\to L}$	2.11	0.78	2.50	2.29	0.97	0.57
$m_{hh,\Gamma\to X}$	0.72	0.89	0.72	1.02	0.65	0.86

TABLE IV. Band gaps, conduction band effective masses $m_{X\to\Gamma}$ and $m_{X\to L}$, light and heavy hole masses m_{lh} and m_{hh} at Γ, and the hole masses at the L point for HfNiSn and HfCoSb, calculated with the PBE, HSE06 density functional, and the GW_0 method.

	HfNiSn			HfCoSb		
functional	PBE	HSE06	GW	PBE	HSE06	GW
$E_{\mathrm{gap}\Gamma-X}$	0.40	0.59	0.97	1.16	1.54	2.06
$E_{\mathrm{gap}L-X}$	0.94	1.36	1.16	1.14	1.73	1.44
$m_{X\to\Gamma}$	2.33	2.17	2.55	3.66	4.11	0.59
$m_{X\to W}$	0.30	0.25	1.01	0.89	0.90	0.49
$m_{lh,\Gamma\to L}$	0.22	0.19	0.20	0.19	0.20	0.35
$m_{lh,\Gamma\to X}$	0.37	0.41	0.30	0.32	0.36	0.73
$m_{h,L\to\Gamma}$	3.92	5.23	1.25	2.74	2.05	1.64
$m_{h,L\to K}$	0.62	0.97	0.88	0.66	0.95	1.06
$m_{hh,\Gamma\to L}$	2.11	1.77	0.54	1.60	1.10	2.62
$m_{hh,\Gamma\to X}$	0.72	0.43	0.32	0.58	0.47	0.54

Ref. [14] are slightly different from ours because they had been evaluated at larger equilibrium lattice constants optimized with the GGA+U method.

The left column of Fig. 2 shows the band structures of ACoSb materials. In the HSE06 functional, all these materials have an indirect band gap $\Gamma \to X$, however, compared to the PBE band gap, it is substantially enlarged. The highest occupied band along $\Gamma - L$ shows only moderate dispersion in both the PBE and the HSE06 functional. However, there are qualitative differences among the materials, but also between the PBE and the HSE06 functional. It should be noted that the fundamental gap of TiCoSb is between the Γ and X point in both functionals, while ZrCoSb has its fundamental gap at $L \to X$ in the PBE functional, in agreement with previous work [20], whereas the HSE06 functional places the VBM always at the Γ point, independent of the group IVb element. The moderately dispersive uppermost valence band along Γ-L originates from π bonding between the metal species along the crystallographic (111) direction. In ZrCoSb, both the Zr and Co d orbitals contribute with similar weight to this band.

TABLE III. Band gaps, conduction band effective masses $m_{X\to\Gamma}$ and $m_{X\to L}$, light and heavy hole masses m_{lh} and m_{hh} at Γ, and the hole masses at the L point for ZrNiSn and ZrCoSb, calculated with the PBE, HSE06 density functional, and the GW_0 method.

	ZrNiSn			ZrCoSb		
functional	PBE	HSE06	GW	PBE	HSE06	GW
$E_{\mathrm{gap}\Gamma-X}$	0.51	0.61	1.04	1.25	1.61	2.03
$E_{\mathrm{gap}L-X}$	0.92	1.35	1.10	1.08	1.63	1.13
$m_{X\to\Gamma}$	3.05	2.17	8.78	4.31	2.17	4.43
$m_{X\to W}$	0.42	0.27	0.94	1.33	0.74	2.18
$m_{lh,\Gamma\to L}$	0.29	0.22	0.20	0.22	0.22	–
$m_{lh,\Gamma\to X}$	0.46	0.36	0.33	0.37	0.32	–
$m_{h,L\to\Gamma}$	2.51	1.38	3.12	2.13	1.61	0.47
$m_{h,L\to K}$	0.99	0.84	2.20	1.08	0.79	0.60
$m_{hh,\Gamma\to L}$	2.09	2.13	0.61	1.85	0.66	–
$m_{hh,\Gamma\to X}$	0.93	0.60	0.96	1.54	0.49	–

This is in contrast to TiCoSb, where the 3d states are too high-lying to mix appreciably with the Co 3d states; hence the uppermost valence band has predominantly Co orbital character in TiCoSb. For this reason, the valence band states in TiCoSb at the Brillouin zone boundary at L have bonding character between Co atoms in adjacent unit cells, different from the corresponding states in ZrCoSb. This explains the different dispersion in the two materials. The role of the functional (PBE versus HSE06) on the dispersion may also be understood on these grounds. In HSE06, the atomic d orbitals are more localized and the energetic position of the d-levels varies more strongly from early to late transition metals. Thus the mixing between the group-IVb orbitals and the Co d orbitals is inhibited when using the HSE06 functional. Remarkably, the conduction band along Γ-X displays stronger dispersion with the HSE06 functional than with the PBE functional. This shows up in the effective masses at the X point valley obtained with the two methods: the conduction band masses are generally lower in HSE06 compared to PBE.

The quasiparticle band structures obtained with the GW_0 approximation are shown in Fig. 3. In the ANiSn materials, the GW_0 band gap is still further increased compared to HSE06. The lowest conduction band in GW_0 shows clearly less dispersion than in the other methods. This results in large effective masses $m_{X\to\Gamma}$ and $m_{X\to W}$ obtained in the GW_0 method. For the ACoSb materials, the gap $\Gamma \to X$ is also increased strongly in the GW_0 method compared to the PBE or HSE06 functionals. However, a remarkable qualitative difference is observed in the valence band: the GW_0 method obtains the VBM at the L point in *all* ACoSb materials; the band L-Γ shows considerable dispersion. This effect is most pronounced in ZrCoSb, where also the smallest band masses $m_{L\to\Gamma}$ and m_{L-K} are found. As a result of the different self-energy corrections to the L and Γ point of the valence band, the fundamental band gap $L \to X$ is smaller in the GW_0 method as compared to the fundamental $\Gamma \to X$ gap in the HSE06 method in the ACoSb materials. In summary, the HSE06 functional is not able to correctly predict the fundamental band gap and band dispersions in case of the ACoSb compounds.

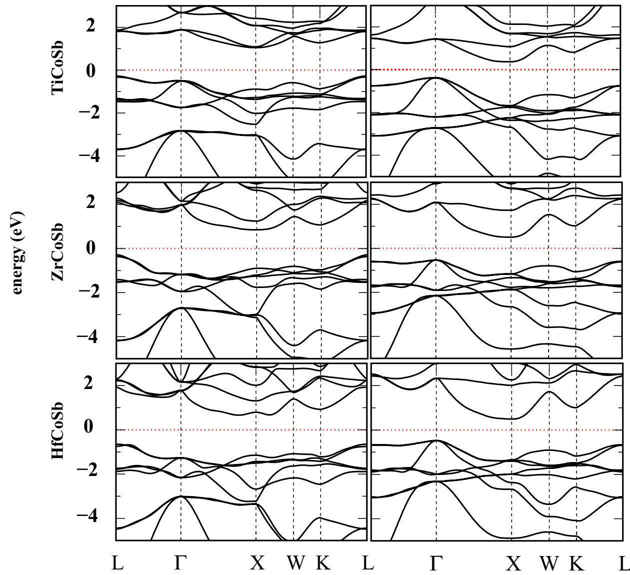

FIG. 3. GW_0 quasiparticle band structures.

B. Thermoelectrics properties

In this section, we aim at an analysis of the Seebeck coefficient and the thermoelectric power factor of the half-Heusler materials. We note that the details of the band structure, including the multiplicity of the extrema and the band curvature (corresponding to the inverse of the transport effective mass) are fully taken into account by our evaluation of thermoelectric quantities with the BOLTZTRAP code [29]. The CBM at the X point leads to six prolate (cigar-shaped) electron pockets, while the VBM at the L point is made up of eight hole pockets. In order to address the role of the effective masses of the carriers, it is, however, required to consider not only the mass in the direction of transport, but also the scattering of the carriers. Calculating the scattering rate from Fermi's golden rule, one finds it to be proportional to the final density of states, and hence to the direction-averaged effective mass $m^* = (m_\parallel m_\perp^2)^{1/3}$, where $m_\parallel$ is the effective mass along the L-Γ or X-Γ direction, and $m_\perp$ is the effective mass in the two directions perpendicular to it. In our analysis, we assume in Eq. (1) an energy dependence of the scattering rate,

$$\tau(E) \sim |E - E_{\mathrm{VBM/CBM}}|^{-1/2}. \tag{2}$$

The exponent $-\frac{1}{2}$ is characteristic of deformation potential scattering by acoustic phonons or alloy scattering. The prevalence of one of these two scattering mechanisms in half-Heusler semiconductors is in agreement with experimental data analysis (see, e.g., Refs. [21,45]). The decrease of the carrier mobility with temperature in ACoSb compounds [18,46] points to at least some contribution of phonons to the total scattering rate. For the prefactor in Eq. (1), we use

$$\tau_0 = 10^{-12}\mathrm{sec}/(m_\parallel^{1/2} m_\perp) \tag{3}$$

with $m_\parallel = m_{X\to\Gamma}$ and $m_\perp = m_{X\to W}$ for the n-type materials. For the p-type materials with the VBM at the L point, $m_\parallel = m_{h,L-\Gamma}$ and $m_\perp = m_{h,L\to K}$ are used, except for the cases where the VBM was obtained at the Γ point, where we approximated $m_\parallel = m_\perp = m_{h,\Gamma\to X}$ instead. The numerical values for each material and computational method were adopted from Tables II–IV. In case of acoustic phonon scattering only, a more precise determination of τ_0 can be obtained [47] by inserting the deformation potential (that has been calculated for some materials [16]) into Fermi's golden rule. Since the rate for alloy scattering is more difficult to estimate, but more important for real materials [21,45], we do not attempt an explicit calculation of the prefactor τ_0, but prefer to stay with the rough estimate given in Eq. (3), which is in line with previous studies [45] attempting to model experimental data.

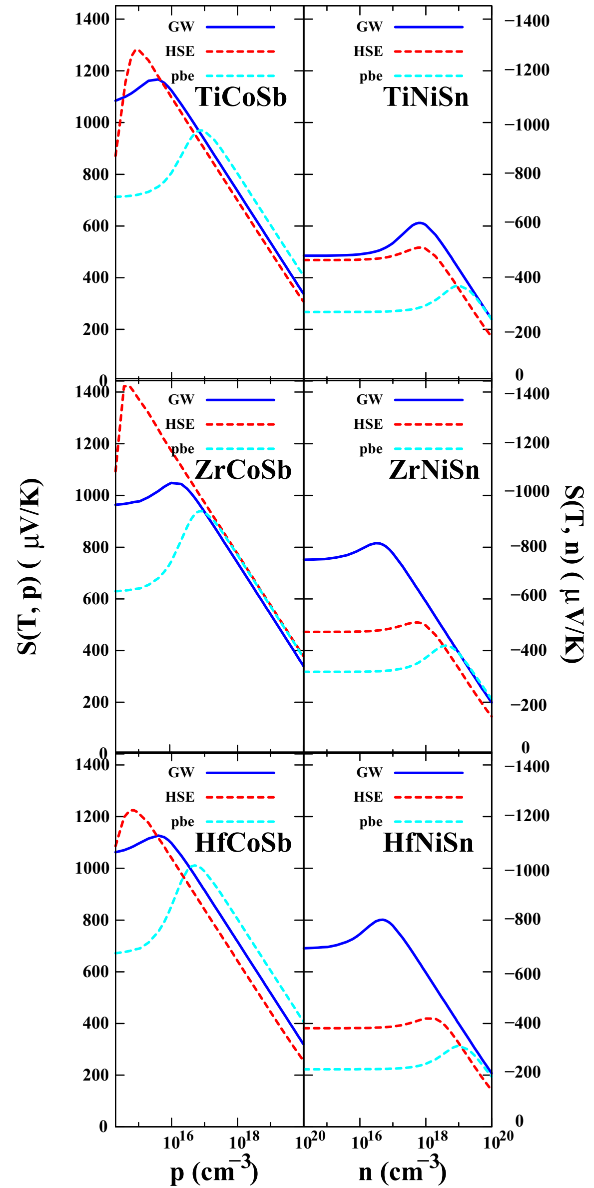

FIG. 4. Seebeck coefficient calculated with various methods at $T = 600$ K using the energy-dependent relaxation time, Eq. (1).

Figure 4 shows the doping dependence of the Seebeck coefficient in all six materials. One can distinguish three regimes: the intrinsic semiconductor at low dopant concentrations, the nondegenerate doped semiconductor, and eventually, at the highest doping concentration, the degenerate (quasimetallic) regime. The cross-over from one regime to the next occurs

at a specific concentration of dopants that depends on the material, but, due to the large differences of band gaps and effective masses found in our first-principles calculations, also on the calculation method. In the intrinsic regime ($n,p \leqslant 10^{15}$ cm^{-3}), the chemical potential of the carriers is located deep in the band gap, and the Seebeck coefficient results from an incomplete compensation of a positive contribution from the hole carriers and a negative contribution from the electrons. The relative weights of these contributions depends on the so-called band weights and thus on the effective masses at both the VBM and CBM. Consequently, the Seebeck coefficients we calculate for this regime are highly method-dependent. At medium doping concentrations, only one type of carriers contributes to the Seebeck coefficient. In line with technical practices, we consider exclusively n-type doping for the ANiSn compounds and exclusively p-type doping for the ACoSb compounds. The absolute thermopower reaches a maximum value in this regime of intermediate doping. At even higher doping concentrations, the chemical potential reaches the conduction band (for n-type doping) or the valence band (for p-type doping). In a degenerate semiconductor ($n,p \geqslant 10^{19}$ cm^{-3}) the thermopower is a decreasing function of the carrier concentration and roughly proportional to $\ln n$ or $\ln p$. In this regime, the dependence of our results on the electronic structure method is less pronounced. We note that the HSE06 functional yields a lower absolute thermopower than the other methods for TiCoSb and HfCoSb. This can be rationalized by observing that the VBM was obtained at the Γ point using the HSE06 functional for these materials, whereas the other methods identify the eightfold degenerate L point as the VBM. Because of this multiplicity of the VBM, a larger $|S|$ is to be expected.

In both the thermoelectric power factor σS^2 and in the dimensionless figure of merit ZT, the electrical conductivity σ enters. While $|S|$ is a decreasing function of the carrier concentration in the degenerate regime, σ linearly increases with carrier concentration. Hence both σS^2 and ZT are expected to display a maximum at some carrier concentration. Moreover, since $\sigma \sim \tau \sim (m_{\parallel}^{1/2} m_{\perp})^{-1}$, the density-of-states effective mass enters inversely into σ. Figure 5 shows the Pisarenko plot, i.e., the power factor σS^2 as a function of carrier concentration at $T = 600$ K for all the six materials considered. Remarkably, the predicted σS^2 curves for each single material show a strong variation with the method of calculation used, while there is less dependence on the group-IVb element within a given method. Specifically for the n-type materials ANiSn, the predicted performance is strongly method-dependent, with HSE06 predicting the largest and the GW_0 method predicting the smallest power factor. This trend is in line with the calculated effective masses in the electron pocket at the X point, with small masses yielding higher power factor. Moreover, it is observed that all σS^2 curves display a maximum for doping concentrations in the range of 10^{19} to 10^{20} cm^{-3}. The precise value of the optimal doping concentration for a given material varies among the different methods used.

For the p-type materials, the maximum power factor is higher than for the n-type materials and the variation of the predicted σS^2 with the method used is somewhat weaker, in particular for TiCoSb. For this material, all methods

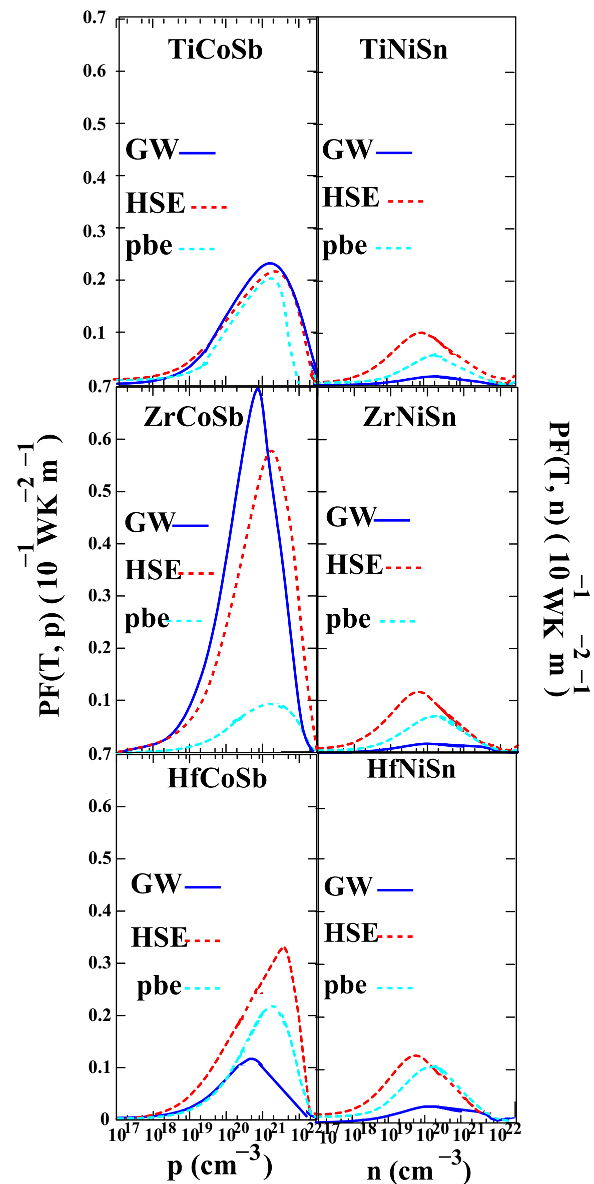

FIG. 5. Thermoelectric power factor calculated with various methods at $T = 600$ K, using the energy-dependent relaxation time, Eq. (1).

predict a maximum power factor of ~0.02 W K^{-2} m^{-1}. For HfCoSb, the GW_0 method predicts a power factor of only 0.01 W K^{-2} m^{-1}. The higher power factor estimated with the HSE06 functional is probably due to the relatively small effective mass $m_{hh,\Gamma\rightarrow X}$ entering the scattering rate in this estimate. The material ZrCoSb is the exception in the sense that the GW_0 method predicts the highest, whereas the PBE functional predicts the lowest power factor among the ACoSb compounds for this material. This can be traced back to the observation that the GW_0 method gave a relatively sharp L-point maximum of the valence band, whereas the effective masses at the L point were larger in PBE, and HSE06 even predicted the VBM to lie at the Γ point. Due to the high hole mobility in ZrCoSb, a power factor up to 0.07 W K^{-2} m^{-1} seems to be achievable in sufficiently pure samples.

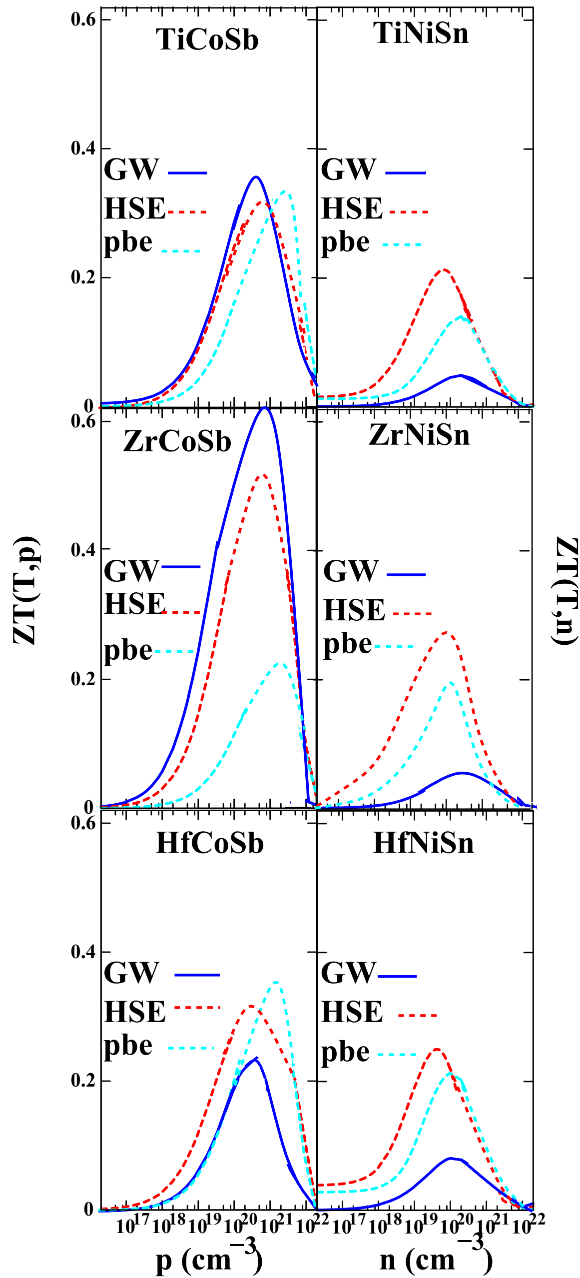

FIG. 6. Figure of merit ZT calculated with various methods at $T = 600$ K, using $\kappa_{\text{lat}} = 20$ W K^{-1} m^{-1}.

Figure 6 shows the figure of merit at $T = 600$ K for all the six materials presented. In addition to the scattering rate of the electronic carriers, a finite material-independent contribution of the lattice to thermal conductivity of $\kappa_{\text{lat}} = 20$ W K^{-1} m^{-1}, taken from recent calculations [9–11] is considered. Although also the electronic contribution to the thermal conductivity is taken into account in calculating ZT, the results are dominated by κ_{lat} at all but the highest doping concentrations. Since under these circumstances the denominator in ZT is nearly constant, the carrier-density dependence due to the electrical conductivity in the numerator plays the most important role. For this reason, the ZT curves in Fig. 6 are qualitatively similar to the power factor curves in Fig. 5. As already discussed above, the materials having a small effective mass in Tables II–IV, and hence a small phase space available for the scattering of the carriers, perform best in our analysis. Again, the ZT values of the n-type materials come out to be method-dependent, but show less variability among TiNiSn, ZrNiSn, and HfNiSn. The maximum of ZT as a function of doping occurs typically between 10^{19} and 10^{20} cm^{-3} at slightly lower carrier concentrations compared to the maximum in σS^2. For low doping concentrations, the n-type materials show a small residual value of ZT due to thermally excited carriers. Generally, the fundamental band gap in the ANiSn materials is less than in the ACoSb materials. The plateaulike ZT level at very small doping concentrations ($<10^{17}$ cm^{-3}) found in different methods correlates inversely with the size of the band gap predicted in this method. This confirms the interpretation of the residual ZT as being due to thermally excited carriers. The variation of the predicted ZT with the method used is weaker for the p-type than for the n-type materials, at least for TiCoSb and HfCoSb. For these two materials, the predicted maximum ZT is in the range of 0.25 to 0.35 for all three methods used. As already observed for the power factor, the material ZrCoSb performs exceptionally well and the GW_0 method predicts a $ZT \sim 0.6$, the highest ZT value of all materials studied here. As already pointed out, in ZrCoSb there is a qualitative difference in the band structure among the methods, whereas the methodological differences in the other materials are quantitative in nature. Indeed, a high figure of merit for ZrCoSb has also been reported experimentally [18].

For practical applications of the materials, the presented ZT values should be understood as conservative estimates. Figures of merit in excess of unity [48] have been obtained experimentally with highly doped and alloyed samples. This is possible because the thermal conductivity of real samples is typically much lower than the 20 W K^{-1} m^{-1} assumed by us, and hence higher ZT values can be reached. First, κ_{lat} is a decreasing function of temperature and drops to values below 10 W K^{-1} m^{-1} at 600 K [12]. Moreover, it is experimentally known that the thermal conductivity is substantially reduced by alloying the half-Heusler materials with a forth chemical species. Recent calculations have shown that mass-disorder scattering is able to bring κ_{lat} down to 3 to 4 W K^{-1} m^{-1} [49], i.e., lowered by a factor of 5 to 6 compared to the ideal crystal. Other methods for reducing the thermal conductivity involve the scattering of phonons by precipitates in samples that display phase separation [19,50], or the scattering of phonons from interfaces in heterostructures [51]. In this way, ZT values larger than unity can be reached.

IV. CONCLUSIONS

In conclusion, our multimethod approach clearly shows that the most elaborate method, i.e., many-body perturbation theory in the form of the GW approach, is required to assess not only the optical, but also the thermoelectric properties of the ternary semiconductors of the half-Heusler family. While the differences in the results of different methods in the n-type materials TiNiSn, ZrNiSn, and HfNiSn affect mostly the maximum value of the figure of merit ZT achievable by doping, for the p-type materials even the position of the valence band maximum in

the Brillouin zone varies among the methods. In the materials TiCoSb, ZrCoSb, and HfCoSb, the GW method locates the maximum at the L point, and the highest thermoelectric power factor is achieved for low eigenvalues of the effective mass tensor if the role of scattering of the carriers for the mobility is taken into account. The location of the valence band maximum obtained with the hybrid functional HSE06 is at variance with both the GW method and the PBE functional. This suggests that HSE06 may be unreliable for half-Heusler materials, and a cross-check with a full GW calculation is recommended. The identification of the material with the best performance in the p-type regime, which we predict to be ZrCoSb, rests on the use of the GW method for the calculation of the effective masses. These findings are expected to guide future high-throughput screening of thermoelectric materials.

ACKNOWLEDGMENTS

We gratefully acknowledge the computing time granted by the Center for Computational Sciences and Simulation (CCSS) of the University of Duisburg-Essen and provided on the supercomputer magnitUDE (DFG Grant No. INST 20876/209-1 FUGG and INST 20876/243-1 FUGG) at the Zentrum für Informations-und Mediendienste (ZIM).

[1] M. Bouhassoune and A. Schindlmayr, Phys. Status Solidi C **7**, 460 (2010).
[2] M. Bouhassoune and A. Schindlmayr, Adv. Condens. Matter Phys. **2015**, 453125 (2015).
[3] P. Rinke, M. Winkelnkemper, A. Qteish, D. Bimberg, J. Neugebauer, and M. Scheffler, Phys. Rev. B **77**, 075202 (2008).
[4] W. Xie, A. Weidenkaff, X. Tang, Q. Zhang, J. Poon, and T. M. Tritt, Nanomaterials **2**, 379 (2012).
[5] S. Bhattacharya and G. K. H. Madsen, J. Mat. Chem. C **4**, 11261 (2016).
[6] P. Gorai, P. Parilla, E. S. Toberer, and V. Stevanović, Chem. Mater. **27**, 6213 (2015).
[7] J. Yan, P. Gorai, B. Ortiz, S. Miller, S. A. Barnett, T. Mason, V. Stevanović, and E. S. Toberer, Energy Envir. Sci. **8**, 983 (2015).
[8] G. D. Mahan and J. O. Sofo, Proc. Natl. Acad. Sci. USA **93**, 7436 (1996).
[9] J. Shiomi, K. Esfarjani, and G. Chen, Phys. Rev. B **84**, 104302 (2011).
[10] J. Carrete, W. Li, N. Mingo, S. D. Wang, and S. Curtarolo, Phys. Rev. X **4**, 011019 (2014).
[11] J. Carrete, N. Mingo, S. D. Wang, and S. Curtarolo, Adv. Funct. Mater. **24**, 7427 (2014).
[12] A. N. Gandi and U. Schwingenschlögl, Phys. Chem. Chem. Phys. **18**, 14017 (2016).
[13] T. Fang, S. Zheng, T. Zhou, L. Yan, and P. Zhang, Phys. Chem. Chem. Phys. **19**, 4411 (2017).
[14] Y. G. Yu, X. Zhang, and A. Zunger, Phys. Rev. B **95**, 085201 (2017).
[15] J. Schmitt, Z. M. Gibbs, G. J. Snyder, and C. Felser, Mater. Horiz. **2**, 68 (2015).
[16] G. Fiedler and P. Kratzer, Phys. Rev. B **94**, 075203 (2016).
[17] G. Joshi, T. Dahal, S. Chen, H. Wang, J. Shiomi, G. Chen, and Z. Ren, Nano Energy **2**, 82 (2013).
[18] T. Sekimoto, K. Kurosaki, H. Muta, and S. Yamanaka, Jap. J. Appl. Phys. **46**, L673 (2007).
[19] E. Rausch, B. Balke, S. Ouardi, and C. Felser, Phys. Chem. Chem. Phys. **16**, 25258 (2014).
[20] G. H. Fecher, E. Rausch, B. Balke, A. Weidenkaff, and C. Felser, Phys. Status Solidi A **213**, 716 (2016).
[21] K. Gałązka, S. Populoh, W. Xie, S. Yoon, G. Saucke, J. Hulliger, and A. Weidenkaff, J. Appl. Phys. **115**, 183704 (2014).
[22] G. Rogl, P. Sauerschnig, Z. Rykavets, V. V. Romaka, P. Heinrich, B. Hinterleitner, A. Grytsiv, E. Bauer, and P. Rogl, Acta Mater. **131**, 336 (2017).
[23] G. Kresse and J. Furthmüller, Phys. Rev. B **54**, 11169 (1996).
[24] G. Kresse and D. Joubert, Phys. Rev. B **59**, 1758 (1999).
[25] J. P. Perdew, K. Burke, and M. Ernzerhof, Phys. Rev. Lett. **77**, 3865 (1996).
[26] J. Heyd, G. E. Scuseria, and M. Ernzerhof, J. Chem. Phys. **118**, 8207 (2003).
[27] J. Heyd, G. E. Scuseria, and M. Ernzerhof, J. Chem. Phys. **124**, 219906 (2006).
[28] A. A. Mostofi, J. R. Yates, G. Pizzi, Y.-S. Lee, I. Souza, D. Vanderbilt, and N. Marzari, Comput. Phys. Commun. **185**, 2309 (2014).
[29] G. K. H. Madsen and D. J. Singh, Comp. Phys. Commun. **175**, 67 (2006).
[30] M.-S. Lee, F. P. Poudeu, and S. D. Mahanti, Phys. Rev. B **83**, 085204 (2011).
[31] K. Durczewski and M. Ausloos, Phys. Rev. B **61**, 5303 (2000).
[32] C. B. H. Evers, C. G. Richter, K. Hartjes, and W. Jeitschko, J. Alloys Compd. **252**, 93 (1997).
[33] P. Villars and L. D. Calvert, *Pearson's Handbook on Crystallographic Data for Intermetallic Phases*, 2nd ed. (ASM international, Materials Park, Ohio, 1991).
[34] S. Öğüt and K. M. Rabe, Phys. Rev. B **51**, 10443 (1995).
[35] J. Paier, M. Marsman, K. Hummer, G. Kresse, I. C. Gerber, and J. G. Angyan, J. Chem. Phys. **124**, 154709 (2006).
[36] A. Zakutayev, X. Zhang, A. Nagaraja, L. Yu, S. Lany, T. O. Mason, D. S. Ginley, and A. Zunger, J. Am. Chem. Soc. **135**, 10048 (2013).
[37] M. Tas, E. Şaşıoğlu, I. Galanakis, C. Friedrich, and S. Blügel, Phys. Rev. B **93**, 195155 (2016).
[38] M. Shishkin and G. Kresse, Phys. Rev. B **74**, 035101 (2006).
[39] M.-S. Lee and S. D. Mahanti, Phys. Rev. B **85**, 165149 (2012).
[40] S. Ouardi, G. H. Fecher, B. Balke, X. Kozina, G. Stryganyuk, C. Felser, S. Lowitzer, D. Ködderitzsch, H. Ebert, and E. Ikenaga, Phys. Rev. B **82**, 085108 (2010).
[41] M. Hichour, D. Rached, R. Khenata, M. Rabah, M. Merabet, A. H. Reshak, S. B. Omran, and R. Ahmed, J. Phys. Chem. Solids **73**, 975 (2012).
[42] D. F. Zou, S. H. Xie, Y. Y. Liu, J. G. Lin, and J. Y. Li, J. Appl. Phys. **113**, 193705 (2013).
[43] D. T. Do, S. D. Mahanti, and J. J. Pulikkoti, J. Phys. Condes. Matter **26**, 275501 (2014).

[44] S. D. Harrington, A. Sharan, A. D. Rice, J. A. Logan, A. P. McFadden, M. Pendharkar, D. J. Pennachio, N. S. Wilson, Z. Gui, A. Janotti, and C. J. Palmstrom, Appl. Phys. Lett. **111**, 061605 (2017).
[45] H. Xie, H. Wang, Y. Pei, C. Fu, X. Liu, G. J. Snyder, X. Zhao, and T. Zhu, Adv. Func. Mater. **23**, 5123 (2013).
[46] X. Yan, G. Joshi, W. Liu, Y. Lan, H. Wang, S. Lee, J. W. Simonson, S. J. Poon, T. M. Tritt, G. Chen, and Z. F. Ren, Nano Lett. **11**, 556 (2011).
[47] C. Herring and E. Voigt, Phys. Rev. **101**, 944 (1956).
[48] S. Chen and Z. Ren, Mater. Today **16**, 387 (2013).
[49] S. N. H. Eliassen, A. Katre, G. K. H. Madsen, C. Persson, O. M. Lovvik, and K. Berland, Phys. Rev. B **95** 045202 (2017).
[50] T. Berry, S. Ouardi, G. H. Fecher, B. Balke, G. Kreiner, G. Auffermann, W. Schnelle, and C. Felser, Phys. Chem. Chem. Phys. **19**, 1543 (2017).
[51] P. Hołuj, C. Euler, B. Balke, U. Kolb, G. Fiedler, M. M. Müller, T. Jaeger, E. C. Angel, P. Kratzer, and G. Jakob, Phys. Rev. B **92**, 125436 (2015).